PAPER

Check for updates

Nonvolatile metal–semiconductor transition of a single valley in two-dimensional ferrovalley/ferroelectric van der Waals heterostructures†

Jianrong Ye,[a] Rongkun Chen, [b] Hua Bai, [ID] *[a] Shiqian Hu [ID] *[b] and Chunhua Zeng*[a]

In valleytronics, achieving nonvolatile control of valley properties remains a significant challenge. In this study, we construct TaNF/Sc$_2$CO$_2$ van der Waals (vdW) heterostructures and investigate their properties using first-principles density functional theory. We demonstrate that by controlling the ferroelectric polarization direction of Sc$_2$CO$_2$, a reversible and nonvolatile transition of a single valley in TaNF from a semiconductor to a metal can be achieved. The heterostructures also exhibit high Curie temperatures, underscoring their potential for practical applications. Furthermore, quantum transport simulations based on two-probe nanodevices confirm that the metal–semiconductor transition is feasible for nonvolatile devices. These findings establish a foundation for ferroelectric control of valleys and present TaNF/Sc$_2$CO$_2$ heterostructures as promising candidates for future spintronic and valleytronic devices.

1. Introduction

Two-dimensional (2D) ferrovalley materials have a wide range of potential application in valleytronic devices due to their spontaneous valley polarization and have also received increasing attention in recent years.[1] As a degree of freedom independent of charge and spin, the valley can be used for information encoding and storage, providing extensive application prospects for low-energy, miniaturized, and novel memory devices.[2–4] Beyond memory applications, ferrovalley materials also hold potential in areas such as quantum computing, valley filters,[5] optoelectronic Hall devices,[6] topological materials and so on.[7–9]

The ability to manipulate valley degrees of freedom, especially the ability to achieve nonequivalent configurations, is critical to advancing spintronics, valleytronics, and high-performance memory devices.[2,10] Various external techniques have been explored for controlling valley polarization. For instance, altering the magnitude of stress can significantly modify the valley polarization,[11–14] and even cause transitions of valley polarization between the valence and conduction bands.[15,16] Magnetic field control is another effective strategy, where changes in the magnetization direction can directly influence the direction of valley polarization.[17–19] Similarly, external electric fields offer control over valley properties,[8,14,20,21]

while doping monolayer materials with specific atoms can tune valley polarization strength.[22,23] Layered materials further provide unique opportunities for valley modulation through interlayer alignment adjustment,[24,25] spacing control,[26] or the introduction of twist angles.[27] However, despite the progress in valley manipulation, many of these techniques are inherently volatile. Valley properties often revert to their original states once external methods are removed, or irreversible structural changes compromise the material's functionality. Therefore, it is necessary to find some nonvolatile control methods to avoid the shortcomings and limitations of the above control methods. Ferroelectric (FE) materials have recently been found to present a viable method for nonvolatile regulation of valley polarization. By reversing the polarization direction of a FE layer, it is possible to achieve valley polarization reversal[9,21] and modulate the magnitude of valley splitting.[28] This method not only enables nonvolatile metal–semiconductor transitions but also creates opportunities for the development of innovative electrical devices.[29–34] However, the realization of metal–semiconductor transitions within a single valley remains a significant challenge.

In this study, we use first-principles density functional theory (DFT) to investigate the electronic properties of a multiferroic vdW heterostructure composed of a ferrovalley monolayer TaNF (TNF)[35] and a FE monolayer Sc$_2$CO$_2$ (SCO).[36] The results show that by adjusting the polarization direction of the SCO layer, the single valley of TNF can be flexibly tuned between semiconductor and metal states. The origin of this transition is a shift in the position of the energy level caused by the change of polarization directions, which alters the charge transfer. In addition, this valley is spin-polarized in the z direction. Monte Carlo (MC) simulations further confirm that the

[a] Faculty of Science, Kunming University of Science and Technology, Kunming 650500, China. E-mail: huabai@kust.edu.cn; chzeng83@kust.edu.cn

[b] School of Physics and Astronomy, Yunnan Key Laboratory for Quantum Information, Yunnan University, Kunming 650091, China. E-mail: shiqian@ynu.edu.cn

† Electronic supplementary information (ESI) available. See DOI: https://doi.org/10.1039/d5na00076a

heterostructures have Curie temperatures (T_C) ranging from 136–209 K, which is crucial for the practical application of nonvolatile spintronic devices. Finally, based on non-equilibrium Green's function (NEGF) transport simulations, we design a TNF/SCO two-terminal nanoscale device, and the results validate that the semiconductor–metal transition in this heterostructure is feasible. Therefore, the TNF/SCO hetero-structure can be used as a switch of current with valley polari-zation and spin polarization. These findings demonstrate an effective way to achieve metal–semiconductor transitions of valleys, provide new ideas for nonvolatile control of valleys, and offer new theoretical guidance for the development of next-generation valleytronic and spintronic devices.

2. Theoretical methodology

In this work, the calculations of structures and electronic prop-erties were performed using the Vienna *ab initio* simulation package (VASP).[37] The generalized gradient approximation (GGA) with the Perdew–Burke–Ernzerhof (PBE)[38] scheme was used for the exchange–correlation function. The electron–ion interaction was described by the projector augmented wave (PAW) method.[39] The plane-wave cutoff energy was set to 400 eV, and a $15 \times 15 \times 1$ Γ-point centered grid was adopted in all calculations. The vdW correction was included using the DFT-D3 method,[40] and dipole correction was applied in all calculations. A vacuum layer of 26 Å perpendicular to the sheets was employed. The force and energy convergence criteria were set to 0.01 eV Å^{-1} and 10^{-5} eV, respectively. The spin–orbit coupling (SOC) was considered in all calculations. The DFT+U method[41] was adopted with Hubbard interaction parameters (U) of 2.1 eV and 3.07 eV for d orbitals of Sc and Ta, respectively. The values of U were obtained from the linear response approach.[42] The climbing image nudged elastic band (CI-NEB) method was used to simulate the ferroelectric transition path.[43] The T_C was obtained from the anisotropic Heisenberg model using the mcsolver package with MC simula-tions.[44] A $32 \times 32 \times 1$ 2D honeycomb grid was used for all MC simulations with the Metropolis algorithm.

The calculations of transmission properties were performed using the Atomistic Simulation Toolkit (ATK)[45] included in the QuantumWise package with NEGF techniques.[46] And two-probe devices with a scattering region of 6 units and an electrode region of 1 unit were used. The energy cutoff was set above 75 Ha, and the OMX PBE pseudopotentials were employed. In the self-consistent calculations, k-point meshes of $161 \times 9 \times 1$ ($x \times y \times z$, x is the transport direction and z is the aperiodic direction) and $8 \times 279 \times 1$ ($x \times y \times z$, y is the transport direction and z is the aperiodic direction) were used for the zigzag and armchair directions, respectively. During the transmission calculations, 51 k-points were sampled along the transport direction.

3. Results and discussion

3.1. Electronic structures of the TaNF monolayer and Sc₂CO₂ monolayer

The structures and electronic properties of the TNF monolayer and SCO monolayer are first investigated. The optimized in-plane lattice constants for TNF and SCO are 3.29 Å and 3.43 Å, respectively, consistent with previous studies.[35,36] The lattice mismatch rate of these two materials is less than 5%, which is suitable for forming a vertical heterostructure. The crystal structure of TNF is shown in Fig. S1(a).† Due to the symmetry breaking caused by different atoms on its two sides, TNF exhibits a spontaneous out-of-plane electric polarization from F to N, and this polarization cannot be reversed. TNF under this polarization is named TNF↑, and the one from N to F is named TNF↓. To ascertain the influence of SOC and magnetism on the valley properties of the TNF monolayer, relevant calculations of band structures are also performed, as shown in Fig. S2.† If SOC is not taken into account, there is no valley polarization in the TNF monolayer, whether in the non-magnetic (NM) state or ferromagnetism (FM) state. When considering SOC, the direc-tion of the magnetic moment becomes very important. To find out the direction of the magnetic moment of the TNF mono-layer, its magnetic anisotropy energy (MAE) is calculated. MAE is the energy difference between in-plane and out-of-plane ferromagnetic states, defined as MAE = $E_y - E_z$, where E_y and E_z represent the energy of the unit cell for in-plane and out-of-plane ferromagnetic directions, respectively. A positive (nega-tive) MAE value indicates that the spin prefers the out-of-plane (in-plane) direction.[47] The result shows that the MAE of the TNF monolayer is 4.7 meV, indicating that its magnetic moment is out of plane. Considering the SOC and the FM state with the out-of-plane magnetic moment direction, the TNF monolayer has a large valley polarization of 339 meV at the K point and $-K$ point, as shown in Fig. S1(c),† and it has a band gap of 255 meV. In addition, when SOC is considered and the TNF monolayer is in the FM state but with the magnetic moment direction in the plane, there is no valley polarization, as shown in Fig. S2(c).† That is to say, SOC and magnetism have a huge impact on the valley properties of the TNF monolayer. Valley polarization only exists below the T_C of FM.

Next, the orbital components of the TNF monolayer near the valley are analyzed. As shown in Fig. S3,† the K valley and $-K$ valley of the TNF monolayer are mainly contributed by the d_{xy} and $d_{x^2-y^2}$ orbitals of Ta and the p_z orbital of F, and the p_x orbital of N also has a small contribution. In addition, the conduction band minimum (CBM) is located at the K valley. The valence band maximum (VBM) is located at the Γ point, and is mainly contributed by the d_{z^2} orbital of Ta and the s orbital of F. Considering the influence of SOC on the distribution of spins in the Brillouin zone, the spin projection bands in the three directions of x, y, and z are also calculated, as shown in Fig. S4.† In the K valley and $-K$ valley, the spins are opposite in the z direction. That is, the two valleys have not only valley polari-zation but also spin polarization in the z direction.

Additionally, SCO is an FE material with out-of-plane polar-ization. Its structure is shown in Fig. S1(b),† consists of a five-layered structure with an O–Sc–C–Sc–O stacking sequence. The asymmetric displacement of the C atomic layer relative to the Sc atomic layer realizes out-of-plane polarization, making the monolayer SCO a 2D FE material. When the C atom is near the top layer or far from the top layer, the polarization state is represented by the letters P↑ and P↓, respectively. Therefore,

SCO is named SCO↑ and SCO↓ according to the direction of polarization. In FE materials, the polarization states in different directions can be reversibly switched by an external electric field, and the polarization state remains even after the external electric field is removed. The band structure of the SCO monolayer, as shown in Fig. S1(d),† reveals a direct bandgap semiconductor with a bandgap of 1.85 eV after considering SOC. The calculation is consistent with the previous article.[32,48] The projected band structure of SCO is shown in Fig. S5.† The calculations reveal that the CBM of SCO is mainly composed of the p_z orbital of C and the s and p_z orbitals of O, while the VBM is composed of the p_x and p_y orbitals of C and the p_y orbital of O.

Although theoretical studies on SCO have been relatively extensive, reports specifically focusing on the calculation of its ferroelectric polarization switching barrier remain scarce. For instance, previous work shows that the polarization reversal barrier for a 2 × 2 supercell of SCO is approximately 2.55 eV.[49] To further verify its polarization behavior, we also calculate the ferroelectric switching barrier in monolayer SCO. As illustrated in Fig. S6(a) and (b),† two paths are considered, named path 1 and path 2. In each path, the green arrow represents the movement direction of the C atoms, while the yellow arrow represents the common movement direction of the lower Sc and O atoms. The polarization switching barriers of the two paths are 0.96 and 0.74 eV, respectively. It is worth noting that in path 2, the SCO monolayer does not strictly follow the reaction pathway we specify. Instead, it automatically optimizes to the intermediate phase depicted in Fig. S6(d).†

3.2. Electronic properties of TNF/SCO vdW heterostructures

Next, the structural and electronic properties of the TNF/SCO heterostructures are investigated. Four heterostructures are established according to the polarization directions of TNF and SCO, respectively: TNF↑/SCO↓ (heterostructure formed by TNF P↑ and SCO P↓), TNF↑/SCO↑, TNF↓/SCO↓, and TNF↓/SCO↑. For each heterostructure, the lower layer of SCO is fixed, and the three sites A, B, and C are considered. As shown in Fig. S7(a),† three stacking options are taken into consideration by shifting the lowest atom of the top material TNF to align the positions A, B, and C accordingly: (i) ① stacking configuration, with F, Ta, and N atoms of TNF sitting at the top-O, top-Sc, and top-C sites of SCO; (ii) ② stacking configuration, with F, Ta, and N atoms of TNF sitting at the top-C, top-O, and top-Sc sites of SCO; (iii) ③

stacking configuration, with F, Ta, and N atoms of TNF sitting at the top-Sc, top-C, and top-O sites of SCO. To find the most suitable stacking model, the cleavage energies of the heterostructures are calculated, defined as E_c. The cleavage energy for TNF/SCO is calculated using the following formula:

$$E_c = \frac{E_{total} - E_{TNF} - E_{SCO}}{A} \tag{1}$$

where E_{total} is the total energy of the TNF/SCO heterostructure, E_{TNF} and E_{SCO} represent the energy of the isolated monolayer TNF and SCO, respectively, and A is the internal area of the primitive cell of the heterostructure. The cleavage energies of the combined systems in various stacking modes are summarized in Table S1.† As expected, the cleavage energies of all heterostructures are negative, demonstrating the stability of the structure and the feasibility of experimentally forming TNF/SCO vdW multiferroic heterostructures. In addition, we find the most stable sequence of TNF/SCO is the ② configuration. This configuration is used for the rest of the calculation. The composition of the four types of heterostructures is shown in Fig. 1.

In the TNF/SCO heterostructure, the optimized in-plane lattice constant is 3.39 Å. Considering the influence of the lattice constant change, the band structures of the TNF monolayer and SCO monolayer under this lattice are first calculated, as shown in Fig. S8.† For the SCO monolayer, a small change in the lattice has almost no effect on the band structure, except that the band gap changes from 1.85 eV to 1.82 eV, while for the TNF monolayer, the change in the lattice opens its band gap from 0.255 eV to 0.43 eV. Next, to study the impact of FE polarization on the electronic structure of TNF, the layer-resolved band structures of the TNF/SCO heterostructure with P↑ or P↓ polarization configurations are calculated, as shown in Fig. 2. The results show that TNF↑/SCO↓ and TNF↓/SCO↓ exhibit semiconductor properties, while TNF↑/SCO↑ and TNF↓/SCO↑ exhibit metallic properties. It is worth noting that in the metallic heterostructures, only a small part of the band near the K valley or −K valley is occupied in the TNF layer. Moreover, in the TNF↑/SCO heterostructure, reversing the polarization direction of SCO leads to a change in the valley polarization of TNF from 286 meV to 394 meV. Similarly, in the TNF↓/SCO heterostructure, the valley polarization increases from 331 meV to 393 meV. Therefore, by controlling the

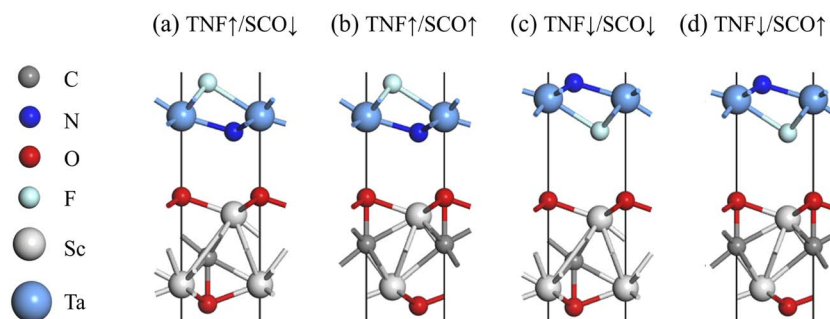**Fig. 1** Side views of the heterostructures: (a) TNF↑/SCO↓, (b) TNF↑/SCO↑, (c) TNF↓/SCO↓ and (d) TNF↓/SCO↑.
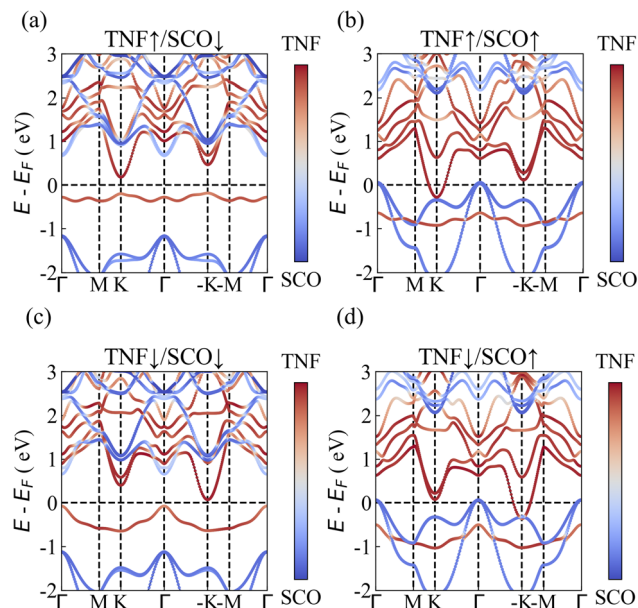
Fig. 2 Band structures of (a) TNF↑/SCO↓, (b) TNF↑/SCO↑, (c) TNF↓/SCO↓ and (d) TNF↓/SCO↑. Where the red and blue represent the contributions of TNF and SCO to the band structure of the heterostructure.

polarization direction of the SCO layer, a nonvolatile occupied/unoccupied state transition of a single valley of the TNF layer can be achieved. That is, a nonvolatile metal–semiconductor transition of a single valley can be realized in the TNF/SCO heterostructures. In addition, as mentioned above, the valley of TNF also has spin polarization in the z direction, so this nonvolatile metal–semiconductor transition has potential application value in valley electronics and spin electronics.

In heterostructures, the change in physical properties caused by polarization reversal of FE materials is often related to the change in interlayer charge transfer.[47,50] Therefore, for the above four heterostructures, the charge transfers between the TNF layer and the SCO layer are also studied. Fig. 3 shows the differential charge density between the two layers of all heterostructures. Yellow and blue represent regions of electron gain and loss, respectively. In order to quantitatively analyze the interlayer charge transfer, the corresponding in-plane averaged differential charge density is also calculated and displayed below each differential charge density image. Furthermore, with the center of the interlayer as the boundary, the in-plane averaged differential charge density on both sides is integrated to obtain the quantitative amount of charge transfer. The results show that in most heterostructures, the charge is transferred from the SCO layer to the TNF layer, except for TNF↓/SCO↓. Moreover, when the polarization direction of SCO points downward (Fig. 3(a) and (c)), the interlayer charge transfer is very small. Considering that the method of calculating charge transfer by differential charge density is not very accurate, this part of the value can be ignored; that is, it can be considered that there is almost no charge transfer between layers. In contrast, when the polarization of SCO is reversed
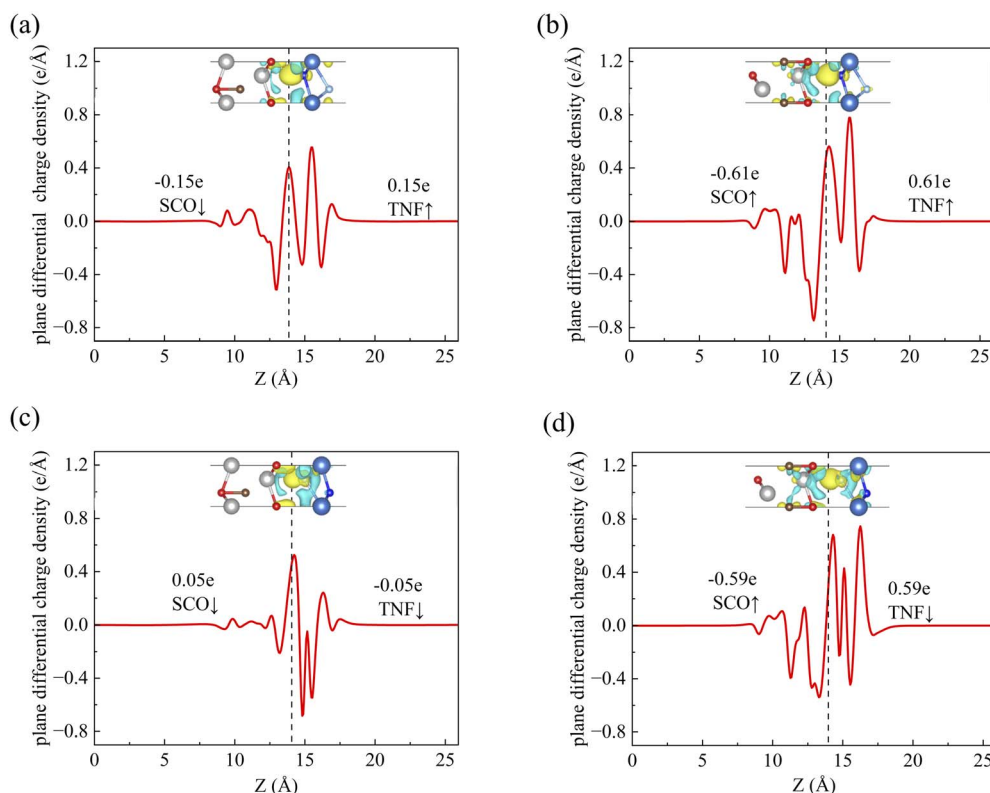

Fig. 3 The differential charge density and corresponding plane differential charge density along the z axis for (a) TNF↑/SCO↓, (b) TNF↑/SCO↑, (c) TNF↓/SCO↓ and (d) TNF↓/SCO↑.

upward (Fig. 3(b) and (d)), a significant interlayer charge transfer occurs within the heterostructure.

The dramatic change in charge transfer caused by the reversal of the polarization direction of the SCO layer is the fundamental reason for the metal–semiconductor transition of the TNF layer. In heterostructures, interlayer charge transfer is often related to the position of the CBM and VBM of the semiconductor or the Fermi level (E_F) of the metal. Electrons tend to transfer from high-energy occupied states to low-energy unoccupied states. To understand this behavior, the band alignments of the TNF monolayer and SCO monolayer in different polarization directions are also calculated. The in-plane averaged electrostatic potentials of SCO and TNF are shown in Fig. 4(a) and (b). Both the TNF monolayer and the SCO monolayer have out-of-plane spontaneous electric polarization, so the electrostatic potential is different on both sides of them. According to the electrostatic potentials and band structures, the VBM and CBM of the TNF monolayer and SCO monolayer in the two polarization directions are rearranged by setting the vacuum energy level to 0, as shown in Fig. 4(c).

When the polarization of SCO points downward (SCO↓), the CBM of SCO↓ is higher than the CBM of both TNF↑ and TNF↓, and the VBM of SCO↓ is much lower than the VBM of both TNF↑ and TNF↓. That is to say, it forms the straddling gap (type I) heterostructure with TNF. In this case, it is difficult to have a charge transfer between SCO and TNF. As a result, both TNF and SCO maintain their semiconducting nature, which leads to the single valley of TNF remaining unoccupied, as shown in Fig. 2(a) and (c). In contrast, when the polarization of SCO flips to the upward direction (SCO↑), the VBM of SCO becomes higher than the CBM of both TNF↑ and TNF↓. In this case, TNF and SCO form the broken gap (type III) heterostructure, which allows easy charge transfer from SCO to TNF. As shown in Fig. 2(b) and (d), charge transfers from the CBM of SCO at the Γ point to the VBM of TNF at the K or $-K$ valley, leading to partial valley occupation, ultimately making TNF metallic. In general, the change in the polarization direction of SCO leads to a change in the heterostructure type, which in turn changes the interlayer charge transfer and ultimately leads to the occurrence of the metal–semiconductor transition.

To elucidate the overall polarization direction of the vdW heterostructure, we systematically analyze the electrostatic potential distribution. As shown in Fig. S9,† the spontaneous

polarization direction of the heterostructure is consistent with the polarization direction of SCO. From the previous electrostatic potential calculation, the difference on both sides of SCO is much larger than that of TNF, which means that the polarization of SCO is much larger than that of TNF, so the overall spontaneous polarization direction of the heterostructure is determined by SCO. From the results, the spontaneous polarization direction of the heterostructure has nothing to do with charge transfer.

Subsequently, to determine the polarization reversal barriers in TNF/SCO heterostructures, we compute the polarization switching pathways for both TNF↑/SCO and TNF↓/SCO configurations based on path 2 of SCO, but in heterostructures, the movement of atoms strictly follows the path we stipulate. As illustrated in Fig. S10(a) and (b),† the polarization reversal barriers are 1.56 eV and 1.59 eV for the respective configurations. The switching barriers obtained here are slightly lower than those reported for analogous Sc₂CO₂-based heterostructures: PtS₂/Sc₂CO₂ heterostructures (1.88 eV)[51] and HfCl₂/Sc₂CO₂ heterostructures (2.01 eV).[52]

3.3. Curie temperature of TNF/SCO vdW heterostructures

As mentioned above, the TNF monolayer exhibits a large valley polarization only in the out-of-plane FM state, so a high T_C is very important for its application as a valley device. Therefore, the T_C of the TNF monolayer and four heterostructures are calculated. In the calculations, the magnetic Hamiltonian is described by the anisotropic Heisenberg model:[44]

$$H = \sum_{m \neq n, \alpha\beta} J_{mn}^{\alpha\beta} S_m^\alpha S_n^\beta + \sum_{m\alpha} D_m^\alpha (S_m^\alpha S_m^\alpha) \qquad (2)$$

The first term represents the exchange interaction between components of spin S_m^α and S_n^β, where $J_{mn}^{\alpha\beta}$ is the magnetic exchange coupling parameter between sites m and n in the magnetic moment directions α and β. The second term describes the single-ion anisotropy, where D_m^α is the magnetic anisotropy parameter of site m in magnetic moment direction α, and α represents the x, y, and z directions. Referring to the method of calculating T_C in previous literature,[53,54] only the diagonal terms in the magnetic exchange coefficient tensor are considered in this calculation, and the nearest neighbor (NN) exchange coupling parameter J_1 and next nearest neighbor
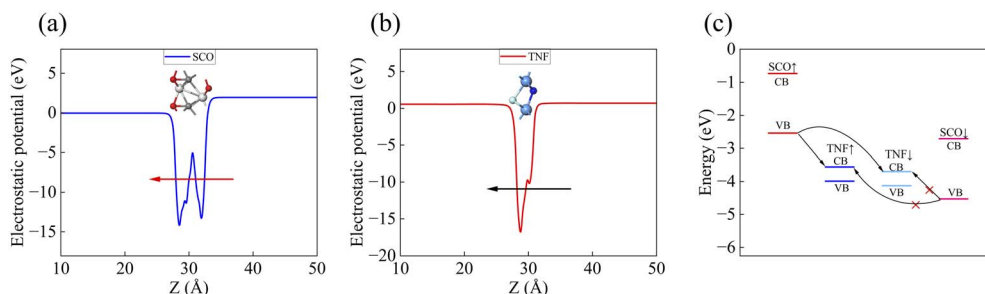

Fig. 4 (a and b) Electrostatic potential of the SCO monolayer and the TNF monolayer, respectively. The arrows in (a) and (b) indicate the polarization direction. (c) Band alignments between TNF and SCO with different polarization directions. Black arrows indicate electron transfer.

Table 1 The MAE and D values of TNF↑/SCO↓, TNF↑/SCO↑, TNF↓/SCO↓ and TNF↓/SCO↑

(meV)	TNF	TNF↑/SCO↓	TNF↑/SCO↑	TNF↓/SCO↓	TNF↓/SCO↑
MAE	4.728	5.579	7.663	4.529	6.457
D	−18.912	−22.316	−30.652	−18.116	−25.828

Table 2 Magnetic exchange coupling parameters in different directions for TNF and the heterostructures

(meV)	J_{1x}	J_{1y}	J_{1z}	J_{2x}	J_{2y}	J_{2z}
TNF	−49.980	−45.497	−56.655	−0.220	−6.767	−1.735
TNF↑/SCO↓	−24.568	−20.304	−30.912	1.927	−4.414	−0.002
TNF↑/SCO↑	−33.315	−29.040	−41.082	0.490	−5.755	−1.957
TNF↓/SCO↓	−40.613	−36.353	−46.193	0.667	−5.508	−1.163
TNF↓/SCO↑	−39.105	−35.405	−45.910	−0.185	−5.575	−2.590

(NNN) exchange coupling parameter J_2 are considered. In this situation, eqn (2) can be written as:

$$H = \sum_{m>n,\alpha} J_1{}^\alpha S_m{}^\alpha S_n{}^\alpha + \sum_{m>n,\alpha} J_2{}^\alpha S_m{}^\alpha S_n{}^\alpha + DS_Z{}^2 \quad (3)$$

In order to obtain the relevant exchange coupling parameters and magnetic anisotropy parameters, we consider three possible magnetic configurations in a $2 \times 3 \times 1$ supercell, three different magnetic configurations are established: FM, ferrimagnetic (FIM), and antiferromagnetic (AFM), as shown in Fig. S11.† Based on the Heisenberg Hamiltonian, the total energies for the three magnetic configurations can be represented as:

$$E_{FM,\alpha} = E_0 + 18J_1S^2 + 18J_2S^2 + DS_Z{}^2 \quad (4)$$

$$E_{FIM,\alpha} = E_0 + 2J_1S^2 - 6J_2S^2 + DS_Z{}^2 \quad (5)$$

$$E_{AFM,\alpha} = E_0 - 6J_1S^2 + 2J_2S^2 + DS_Z{}^2 \quad (6)$$

DFT calculated magnetic moments are $1\mu_B$/Ta, indicating that magnetic Ta possesses a spin $S = \frac{1}{2}$. And D is obtained from the MAE calculation:

$$D = -\frac{E_y - E_z}{(S)^2} = -\frac{MAE}{(S)^2} = -4MAE \quad (7)$$

The MAE of each heterostructure is shown in Table 1, indicating that the magnetic moments of Ta atoms in these four heterostructures are all out-of-plane, which is consistent with those in the TNF monolayer. Next, the magnetic exchange coupling parameters J_1 and J_2 of the TNF monolayer and the four heterostructures are calculated, as shown in Table 2. The subscripts x, y, and z represent the exchange coefficients in the x, y, and z directions, respectively.

Using the above calculation results, the T_C of the TNF monolayer and the four heterostructures are calculated by the
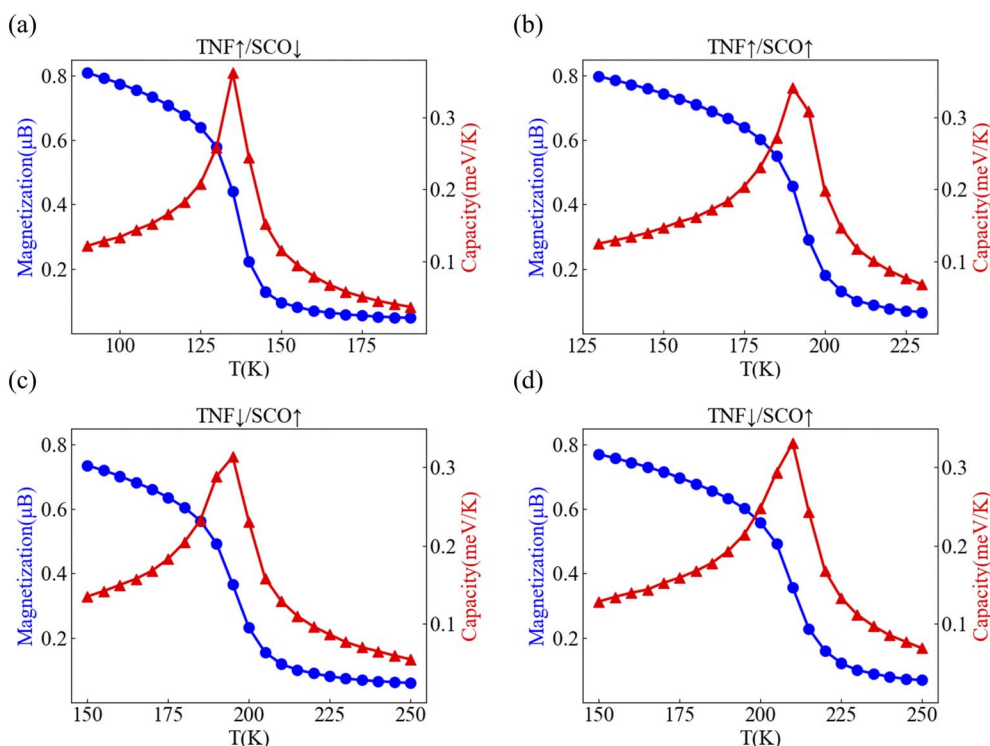
Fig. 5 Temperature variation of the magnetization and capacity for (a) TNF↑/SCO↓, (b) TNF↑/SCO↑, (c) TNF↓/SCO↓ and (d) TNF↓/SCO↑.

MC method. Fig. 5 and S12† show the temperature dependence of the magnetization and capacity for the four heterostructures and the TNF monolayer, respectively. The T_C of the TNF monolayer is calculated to be 236 K, which is close to the results reported in previous literature. For the four heterostructures: TNF↑/SCO↓, TNF↑/SCO↑, TNF↓/SCO↓, and TNF↓/SCO↑, their T_C are 136 K, 191 K, 194 K and 209 K, respectively. Although these heterostructures have relatively high T_C, they are still a little bit away from room temperature, and further research is needed to enable them to reach room temperature.

3.4. Transport properties of TNF/SCO nonvolatile valley metal–semiconductor transition nanodevices

Considering the potential application of the nonvolatile metal–semiconductor transition of the valley in the TNF/SCO heterostructure for nanodevices, its transport properties are further calculated. In transport calculations, supercells of $1 \times \sqrt{3}$ are used, as shown in Fig. S13(a).† In addition, both zigzag and armchair directions are considered in the calculation. As shown in Fig. S13(b) and (c),† a dual-probe device is constructed based on the zigzag and armchair directions. Fig. 6 shows the transmission spectra of the heterostructures for TNF↑ in the zigzag and armchair directions. The corresponding transport properties at E_F are also summarized in Table 3. From the results, whether in the zigzag or armchair direction, the change in the

Table 3 Summary of transmission data for the TNF↑/SCO heterostructure along the zigzag and armchair directions, including the transmission, TER, and RA

	Zigzag		Armchair	
	TNF↑/SCO↓	TNF↑/SCO↑	TNF↑/SCO↓	TNF↑/SCO↑
T	0	0.29	0	5.97
RA (Ω μm^2)	∞	2.47×10^{-2}	∞	2.08×10^{-3}
TER	∞		∞	

electric polarization direction of SCO brings great changes to the transport properties of the heterostructures. When SCO is in the P↓ state, the transmission of the heterostructures near E_F is 0, and when SCO is in the P↑ state, the heterostructures exhibit larger transmission near E_F. This is a natural consequence of the metal–semiconductor transition in the heterostructures.

The phenomenon where FE polarization reversal brings about a huge change in transmission is common in ferroelectric tunnel junctions (FTJs). Although the TNF/SCO heterostructure is not an FTJ, since they have similar properties, the relevant performance is also calculated with reference to the FTJ. Analogous to the tunneling electroresistance in FTJs, in the TNF/SCO heterostructure, we define the transmission electroresistance (TER), with the TER ratio given by:
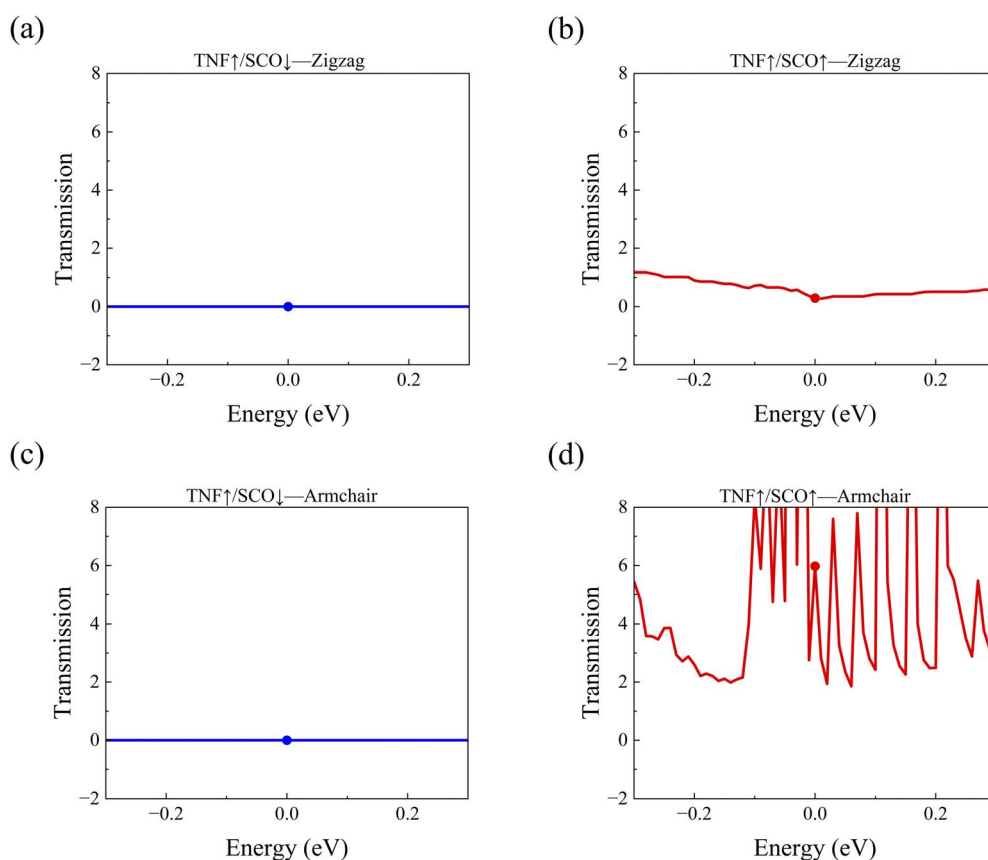
Fig. 6 Transmission spectrum of the TNF↑/SCO heterostructure along the zigzag direction for (a) SCO↓ and (b) SCO↑. Transmission spectrum of the TNF↑/SCO heterostructure along the armchair direction for (c) SCO↓ and (d) SCO↑.
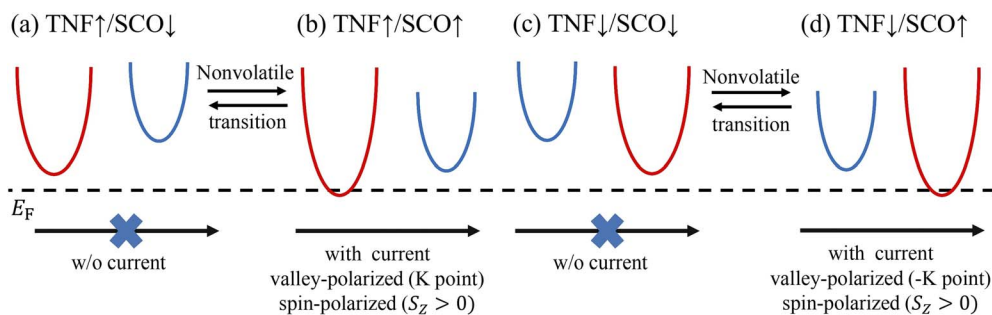
Fig. 7 Working principle diagram of the two-electrode device. (a) TNF↑/SCO↓, (b) TNF↑/SCO↑, (c) TNF↓/SCO↓, and (d) TNF↓/SCO↑. The dashed lines represent the Fermi level. Red and blue indicate $S_Z > 0$ and $S_Z < 0$, respectively.

$$\text{TER} = \frac{T_\uparrow - T_\downarrow}{T_\downarrow} \qquad (8)$$

where $T_\uparrow$ and $T_\downarrow$ represent the transmission at E_F for the SCO layer in the P↑ state and P↓ state, respectively. According to this definition, the TER of the TNF/SCO heterostructure is infinite since $T_\downarrow$ is 0 in all cases, representing a complete metal–semiconductor transition.

Next, the resistance area (RA) product is also calculated (the detailed calculation process is provided in Section 1 of the ESI†). For a multi-resistance state device, in the low-resistance state, the smaller the RA product is, the better. Conversely, in the high-resistance state, the larger the RA product is, the better. This is more advantageous in information storage applications. For example, with a recording density of approximately 200 Gbit per in^2, the RA product should be less than 1 Ω μm^2.[55] The results show that, whether in the zigzag direction or the armchair direction, in the TNF↑/SCO↑ heterostructure, the RA product is very small: it reaches 2.47×10^{-2} Ω μm^2 in the zigzag direction and 2.08×10^{-3} Ω μm^2 in the armchair direction, respectively. When the electric polarization direction of SCO is flipped downward, the RA product becomes infinite. This is in line with the above-mentioned memory device requirements for the RA product. The same calculations are performed for the two heterostructures related to TNF↓; their transmission spectra are shown in Fig. S14,† and the corresponding transport properties at E_F are summarized in Table S2.† All the calculation results are very similar to those of the heterostructures related to TNF↑.

Since the conductivity is proportional to the transmission at E_F, the conductance value can also be computed using the Landauer formula employing the transmission coefficients T_{E_F} at E_F, as shown in eqn (9):[56]

$$G = \frac{2q^2}{h} T_{E_F} \qquad (9)$$

where G represents electrical conductivity, q is the charge of an electron, and h is Planck's constant. Therefore, for the two polarization states of SCO, when the polarization is downward, G is 0, which is a non-conductive state. When SCO turns into a polarization upward state, G of the device is greater than 0, and the device is in a conductive state. According to the above calculation results, the TNF/SCO heterostructure can be used as a metal–semiconductor transition nanodevice. Nonvolatile control of the current can be achieved by varying the polarization direction of the FE layer. We further explain its working principle with Fig. 7. In TNF↑/SCO↓, both K and $-K$ valleys are higher than E_F (Fig. 7(a)), and there is no current in the device. However, in TNF↑/SCO↑, only the K valley passes through E_F (Fig. 7(b)), and there is a valley-polarized and spin-polarized ($S_Z > 0$) current in the device. Moreover, the above two states can be switched in a nonvolatile manner by the electric polarization direction of SCO. Similar relationships exist in TNF↓/SCO↓ and TNF↓/SCO↑ (Fig. 7(c) and (d)). That is, the TNF/SCO heterostructure can be used as a switch of current with valley polarization and spin polarization.

4.   Conclusion

In summary, we have investigated the electronic properties and transport properties of TNF/SCO multiferroic vdW heterostructures using DFT and NEGF. Our findings reveal a nonvolatile transition in which the single valley of TNF can be switched between the semiconductor state and the metal state by modulating the FE polarization. This transition is driven by polarization-induced shifts in energy levels, which alter the charge transfer within the heterostructure. These results demonstrate the significant potential of TNF/SCO heterostructures for applications in spintronic and valleytronic nanodevices, such as a switch of current with valley polarization and spin polarization, providing a promising platform for developing high-performance, nonvolatile memory and logic devices. Moreover, this work offers new insights into the interplay between ferrovalley and ferroelectric materials, and provides new theoretical guidance for future multiferroic materials and devices.

Data availability

The data supporting the findings of this study are available within the article and its ESI files.† Additional datasets generated during the study, including computational input files and analysis scripts, are available from the corresponding author upon reasonable request.

Conflicts of interest

There are no conflicts to declare.

Acknowledgements

References

1 Y.-Y. Sun, L. Shang, W. Ju, Y.-P. An, S.-J. Gong and J.-Q. Wang, *J. Mater. Chem. C*, 2019, **7**, 14932–14937.

2 R. Peng, Z. He, Q. Wu, Y. Dai, B. Huang and Y. Ma, *Phys. Rev. B*, 2021, **104**, 174411.

3 T. Zhang, X. Xu, B. Huang, Y. Dai and Y. Ma, *npj Comput. Mater.*, 2022, **8**, 64.

4 S. Li, Y. Hou, M. Zhou, F. Zheng, X. Shao and P. Zhang, *J. Appl. Phys.*, 2023, **134**, 213901.

5 B. Zhou, Z. Li, J. Wang, X. Niu and C. Luan, *Nanoscale*, 2019, **11**, 13567–13575.

6 T. Cao, G. Wang, W. Han, H. Ye, C. Zhu, J. Shi, Q. Niu, P. Tan, E. Wang, B. Liu and J. Feng, *Nat. Commun.*, 2012, **3**, 887.

7 C. Shen, G. Wang, T. Wang, C. Xia and J. Li, *Appl. Phys. Lett.*, 2020, **117**, 042406.

8 D. Zhang, Y. Zhang and B. Zhou, *Nanoscale*, 2023, **15**, 1718–1729.

9 C. Lei, X. Li, Y. Ma and Z. Qian, *Phys. Rev. B*, 2023, **108**, 155431.

10 S. Shrestha, M. Li, S. Park, X. Tong, D. DiMarzio and M. Cotlet, *Nat. Commun.*, 2023, **14**, 5234.

11 S.-D. Guo, X.-S. Guo, X.-X. Cai and B.-G. Liu, *Phys. Chem. Chem. Phys.*, 2022, **24**, 715–723.

12 H.-X. Cheng, J. Zhou, W. Ji, Y.-N. Zhang and Y.-P. Feng, *Phys. Rev. B*, 2021, **103**, 125121.

13 M. Lan, Y. Li, S. Qiao, T. Huang, S. Ma, F. Ding, H. Wu, F. Li and Y. Pu, *J. Phys. D: Appl. Phys.*, 2023, **56**, 385103.

14 L. Wang, Z. Lin and Y. An, *J. Alloys Compd.*, 2021, **854**, 157141.

15 M.-Y. Liu, G.-Q. Li, Y. He and K. Xiong, *Phys. Chem. Chem. Phys.*, 2024, **26**, 2341–2354.

16 K. Jia, X.-J. Dong, S.-S. Li, W.-X. Ji and C.-W. Zhang, *Nanoscale*, 2024, **16**, 8639–8649.

17 P. Back, M. Sidler, O. Cotlet, A. Srivastava, N. Takemura, M. Kroner and A. Imamoğlu, *Phys. Rev. Lett.*, 2017, **118**, 237404.

18 B. Zhai, R. Cheng, W. Yao, L. Yin, C. Shen, C. Xia and J. He, *Phys. Rev. B*, 2021, **103**, 214114.

19 C. Li and Y. An, *Phys. Rev. B*, 2022, **106**, 115417.

20 Y. Li, Y. Wu, L. Deng, X. Yin, X. Han, F. Tian and X. Zhang, *J. Appl. Phys.*, 2023, **133**, 134301.

21 H. Hu, W.-Y. Tong, Y.-H. Shen and C.-G. Duan, *J. Mater. Chem. C*, 2020, **8**, 8098–8106.

22 L. Zhong, X. Chen and J. Qi, *Phys. Chem. Chem. Phys.*, 2017, **19**, 15388–15393.

23 Y. C. Cheng, Q. Y. Zhang and U. Schwingenschlögl, *Phys. Rev. B: Condens. Matter Mater. Phys.*, 2014, **89**, 155429.

24 Q. Zhang, S. A. Yang, W. Mi, Y. Cheng and U. Schwingenschlögl, *Adv. Mater.*, 2016, **28**, 959–966.

25 C. Wang and Y. An, *Appl. Surf. Sci.*, 2021, **538**, 148098.

26 X. Zhang, K. Zhang, Y. Zhu, B. Zhou and X. Wang, *Phys. Chem. Chem. Phys.*, 2024, **26**, 27922–27932.

27 L. Li, X. Li, L. Lin, D. Zhang, M. Chen, D. Wu and Y. Yang, *Phys. Rev. B*, 2024, **110**, 205119.

28 F. Yang, J. Shang, L. Kou, C. Li and Z. Deng, *Nanomaterials*, 2022, **12**, 2461.

29 Z. He, R. Peng, X. Feng, X. Xu, Y. Dai, B. Huang and Y. Ma, *Phys. Rev. B*, 2021, **104**, 075105.

30 X. Yang, N. Ding, J. Chen, Z. Wang, M. An and S. Dong, *Appl. Phys. Lett.*, 2023, **122**, 162403.

31 G. Liu, T. Chen, G. Zhou, Z. Xu and X. Xiao, *ACS Sens.*, 2023, **8**, 1440–1449.

32 G. Liu and S.-H. Ke, *Nano Lett.*, 2024, **24**, 10776–10782.

33 G. G. Liu and S. H. Ke, *Phys. Rev. Appl.*, 2024, **21**, 044033.

34 G. G. Liu, Z. H. Xu, X. B. Xiao and S. H. Ke, *Phys. Rev. B*, 2024, **109**, 155418.

35 G. Zheng, S. Qu, W. Zhou and F. Ouyang, *Front. Phys.*, 2023, **18**, 53302.

36 Y. Zhao, J.-J. Zhang, S. Yuan and Z. Chen, *Adv. Funct. Mater.*, 2019, **29**, 1901420.

37 G. Kresse and J. Furthmüller, *Comput. Mater. Sci.*, 1996, **6**, 15–50.

38 J. Heyd, G. E. Scuseria and M. Ernzerhof, *J. Chem. Phys.*, 2003, **118**, 8207–8215.

39 P. E. Blöchl, *Phys. Rev. B: Condens. Matter Mater. Phys.*, 1994, **50**, 17953–17979.

40 S. Grimme, J. Antony, S. Ehrlich and H. Krieg, *J. Chem. Phys.*, 2010, **132**, 154104.

41 S. L. Dudarev, G. A. Botton, S. Y. Savrasov, C. J. Humphreys and A. P. Sutton, *Phys. Rev. B: Condens. Matter Mater. Phys.*, 1998, **57**, 1505–1509.

42 M. Cococcioni and S. de Gironcoli, *Phys. Rev. B: Condens. Matter Mater. Phys.*, 2005, **71**, 035105.

43 G. Henkelman, B. P. Uberuaga and H. Jónsson, *J. Chem. Phys.*, 2000, **113**, 9901–9904.

44 L. Liu, X. Ren, J. Xie, B. Cheng, W. Liu, T. An, H. Qin and J. Hu, *Appl. Surf. Sci.*, 2019, **480**, 300–307.

45 S. Smidstrup, T. Markussen, P. Vancraeyveld, J. Wellendorff, J. Schneider, T. Gunst, B. Verstichel, D. Stradi, P. A. Khomyakov, U. G. Vej-Hansen, M.-E. Lee, S. T. Chill, F. Rasmussen, G. Penazzi, F. Corsetti, A. Ojanperä, K. Jensen, M. L. N. Palsgaard, U. Martinez, A. Blom, M. Brandbyge and K. Stokbro, *J. Phys.: Condens. Matter*, 2020, **32**, 015901.

46 M. Brandbyge, J.-L. Mozos, P. Ordejón, J. Taylor and K. Stokbro, *Phys. Rev. B: Condens. Matter Mater. Phys.*, 2002, **65**, 165401.

47 H. Bai, X. Li, H. Pan, P. He, Z.-a. Xu and Y. Lu, *ACS Appl. Mater. Interfaces*, 2021, **13**, 60200–60208.

48 L. Cao, X. Deng, G. Zhou, S.-J. Liang, C. V. Nguyen, L. K. Ang and Y. S. Ang, *Phys. Rev. B*, 2022, **105**, 165302.

49 W. R. Liu, X. J. Dong, Y. Z. Lv, W. X. Ji, Q. Cao, P. J. Wang, F. Li and C. W. Zhang, *Nanoscale*, 2022, **14**, 3632–3643.

50 H. Bai, X. Wang, W. Wu, P. He, Z. A. Xu, S. A. Yang and Y. Lu, *Phys. Rev. B*, 2020, **102**, 235403.

51 Y. Zhang, Y. Shen, L. Lv, M. Zhou, X. Yang, X. Meng, N. Zhang, K. Wang, B. Zhang and Z. Zhou, *Phys. Rev. Appl.*, 2023, **20**, 044066.

52 Z. Cui, X. Duan, J. Wen, Z. Zhu, J. Zhang, J. Pei, C. Wen, T. Zhou, B. Wu and B. Sa, *Appl. Phys. Lett.*, 2025, **126**, 122902.

53 F. Azizi and H. Rezania, *ECS J. Solid State Sci. Technol.*, 2021, **10**, 081012.

54 A. Pokhriyal, A. Ghosh and H. Ghosh, *J. Phys. Chem. Solids*, 2023, **172**, 111085.

55 Y. Nagamine, H. Maehara, K. Tsunekawa, D. D. Djayaprawira, N. Watanabe, S. Yuasa and K. Ando, *Appl. Phys. Lett.*, 2006, **89**, 162507.

56 M. Büttiker, Y. Imry, R. Landauer and S. Pinhas, *Phys. Rev. B: Condens. Matter Mater. Phys.*, 1985, **31**, 6207–6215.